

Exploring Photometry System Trades with a Pixel-Level Data Simulator

Nicole Gagnier, Brandoch Calef

The Boeing Company

Ryan Coder

Air Force Research Laboratory

ABSTRACT

In this paper, we present a pixel-level data simulator for space object characterization studies. We outline the development and testing of the tool including comparisons to on-sky data collected at the Maui Space Surveillance site. We describe key performance metrics for a space situational awareness sensor and provide theoretical expressions that predict such metrics. Finally, we evaluate the metrics using the simulator over various parameters or trades demonstrating the ability to discover trends and effects not captured by theory alone.

Keywords: Photometry, simulated imagery, design space exploration

1. INTRODUCTION

The characterization of space objects is influenced by a vast array of collection system characteristics, including camera noise, spatial pixel sampling, optical aberrations, the distribution of reference stars in the field of view, telescope mount jitter, and so on. As more of these real-world effects are taken into consideration, it becomes essentially impossible to write down a closed-form expression that quantifies performance. Furthermore, one may define “performance” in different ways, such as limiting magnitude, photometric uncertainty, or metric accuracy, and look for sensor designs that trade off these objectives in an optimal way.

In this paper, we describe a pixel-level simulation tool and share the results of some system design space exploration that we have undertaken. The simulator is built upon SkyMaker, a highly detailed code from the astronomical community, and extends it to address satellite observation scenarios. It has been validated against on-sky data collected by sensors at the Maui Space Surveillance Site (MSSS). Using the simulator, we show how photometric and astrometric uncertainty diverges from textbook predictions as real-world effects are modeled. We illustrate how sensor performance may be optimized over a range of design choices and operation modes.

2. SIMULATOR DESIGN AND IMPLEMENTATION

The simulator consists of two main components, one to define and iterate over the parameter space (i.e. combinations of target and sensor characteristics), and one to generate and save data for subsequent analysis. The simulator is written in Python and uses multiprocessing at the frame level to maximize speed when generating data.

The simulator accounts for a wide range of real-world phenomena. SkyMaker, the software package upon which the simulator is built, specifically models point spread function effects including atmospheric blurring, telescope motion blurring, instrument diffraction and aberrations, optical diffusion, and intra-pixel response in addition to modeling sky background, noise, saturation, and quantization effects [1]. The simulator also captures photometric effects due to star field density and star streaking while tracking an object. The simulator does not attempt to model weather, stochastic atmospheric turbulence, or complex mount jitter modes.

DISTRIBUTION A. Approved for public release: distribution unlimited.

2.1 SkyMaker

The simulator is built on the open source software package SkyMaker, which simulates astronomical images at the pixel level [1]. SkyMaker models a wide array of camera and sky phenomena such as telescope spider obscurations and mirror size, sky background, and saturation effects as mentioned above. To make use of the SkyMaker code, we created a Python interface to its internal functions. This allows us to manipulate the image frames produced by SkyMaker to account for effects that it does not natively support, such as streaking effects due to mount slewing. SkyMaker could not effectively handle star streaks produced by tracking satellite objects with longer exposure times so it was crucial to add this capability to the simulator.

2.2 Processing Simulated Data

In order to determine performance metrics from the simulated data, we use a combination of SExtractor [2] and Astrometry.net [3] to extract the sources from the simulated data, solve the star field, and determine the coordinate transformations between pixels in the image to right ascension and declination. From this, one can estimate position (in celestial coordinates) and calibrated magnitude for each of the sources detected in the field.

3. TESTING AND VALIDATION OF SIMULATOR OUTPUT

The simulator's output was validated against input truth (including line-of-sight astrometric accuracy, target magnitude, star positions and magnitudes, and zero point) while adjusting instantaneous field of view (IFOV), integration time, and other system characteristics. As a further sanity check, we visually compared its output to (real) sensor data as illustrated in Fig. 1 and 2.



Figure 1: Sensor data collected from MSSS (left) vs. simulated data (right) of star field (RA 297.82°, Dec 7.39°).

4. PERFORMANCE METRICS

Three basic performance measures for space object characterization are metric accuracy, photometric accuracy, and limiting magnitude for detection. A search-oriented mission may be willing to sacrifice metric accuracy for an increase in limiting magnitude in order to detect more objects. A different mission focused on change detection may place higher weight on photometric accuracy to track changes in the object's light curve over time and accordingly tune the system for a specific range of magnitudes, sacrificing detection of dimmer objects. For this paper, we look at these three metrics and compare theory-based predictions with simulated data over a range of input parameters.



Figure 2: Sensor data collected from MSSS (left) vs. simulated data (right) of star field (RA 270.58°, Dec 24.70°).

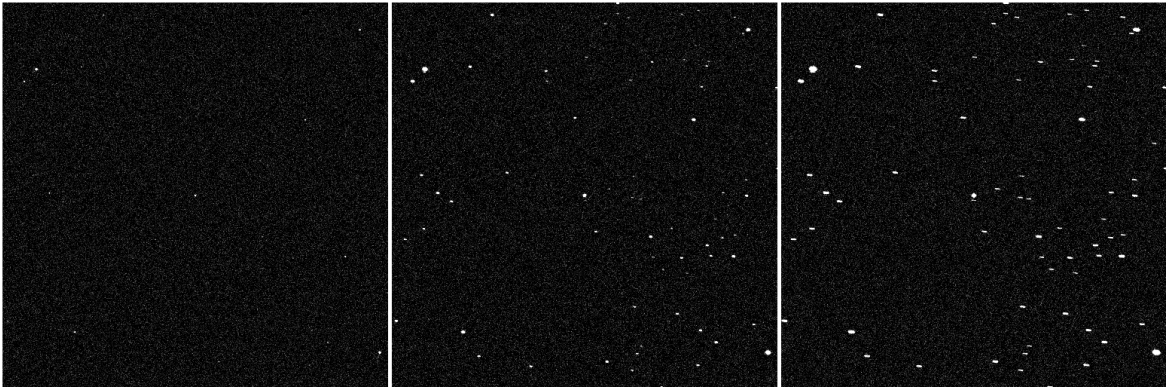


Figure 3: Simulated data of GEO satellite with integration time of 0.1 (left), 0.5 (middle), and 1.0 (right) seconds.

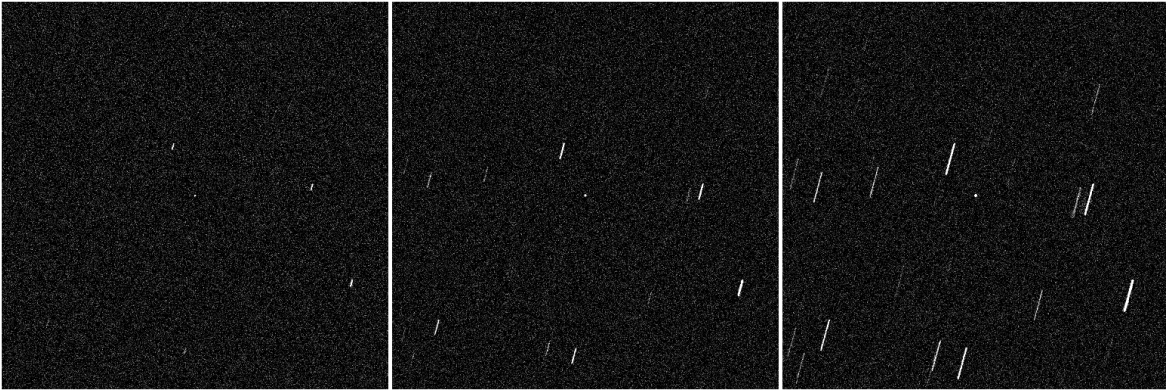


Figure 4: Simulated data of LEO satellite with integration times of 0.1 (left), 0.25 (middle), and 0.5 (right) seconds.

4.1 Photometric Accuracy

The photometric uncertainty (standard deviation of the estimated apparent magnitude) for a given observation is [4]

$$\sigma_{\text{photo}} = \sqrt{\sigma_*^2 + \sigma_{z_p}^2}, \quad (1)$$

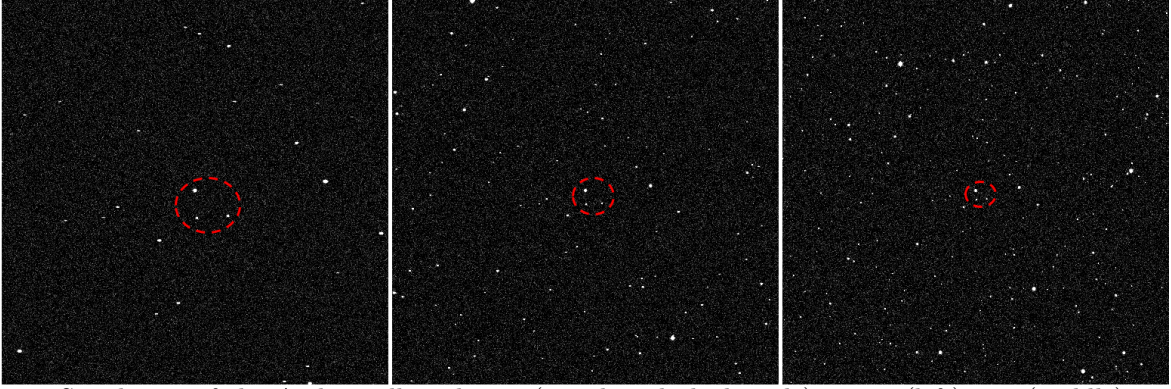


Figure 5: Simulation of the Anik satellite cluster (noted in dashed circle) at 2.0 (left), 4.0 (middle), and 6.0 (right) arcsecond IFOV.

where σ_*^2 is the variance of the instrumental magnitude and σ_{zp}^2 is the variance for the zero point estimate. It can be shown that on average, $\sigma_{zp}^2 = 149.1 \times 10^{-0.4M_{zp}} / (\theta_{\text{FOV}}^2 \Delta t)$, where θ_{FOV} is the field of view in degrees and M_{zp} is the zero point. This contribution to the photometric error is typically much smaller than σ_* . The error in instrumental magnitude is related to the signal-to-noise ratio (SNR) of the measured photoelectrons on the detector by

$$\sigma_* = 1.0857/\text{SNR}, \quad (2)$$

where the 1.0857 factor emerges from the conversion to magnitudes [5].

The SNR of an aperture-photometry style flux measurement using a charge coupled device (CCD) camera is given by [6]

$$\text{SNR} = \frac{N_*}{\sqrt{N_* + n_{\text{pix}}(N_S + N_D + N_R^2)}}, \quad (3)$$

where N_* is the mean number of photoelectrons collected in the source, n_{pix} is the total number of pixels in the extraction aperture, N_S is the sky background level in electrons per pixel per integration, N_D is the dark level in electrons per pixel per integration, and N_R^2 is the read noise standard deviation in RMS electrons per pixel. Most modern CCD cameras are cooled to the point where dark noise is negligible, so N_D is taken to be 0.

Evaluating the “best-case” SNR and σ_* requires finding the optimum extraction aperture size. For this, it is first necessary to have the size of the point-spread function. The full-width half-max (FWHM) of a Gaussian distribution with standard deviation σ is [7]

$$\text{FWHM} = \sigma\sqrt{8 \ln 2} \quad (4)$$

For Gaussians f and g having variance σ_f^2 and σ_g^2 , respectively, the convolution $f * g$ has variance $\sigma_{(f*g)}^2$, given by [8]

$$\sigma_{(f*g)}^2 = \sigma_f^2 + \sigma_g^2. \quad (5)$$

By Eqns. 4 and 5,

$$\text{FWHM}_{(f*g)} = \sqrt{\text{FWHM}_f^2 + \text{FWHM}_g^2}. \quad (6)$$

The point spread function (PSF) is modeled as the convolution of the diffraction limited PSF, the atmospheric seeing PSF, and the jitter PSF, so

$$\text{FWHM}_{\text{PSF}} \approx \text{FWHM}_{(\text{diff*seeing*jitter})} \approx \sqrt{\text{FWHM}_{\text{diff}}^2 + \text{FWHM}_{\text{seeing}}^2 + \text{FWHM}_{\text{jitter}}^2}, \quad (7)$$

where $\text{FWHM}_{\text{diff}}$ is the diffraction limited FWHM, $\text{FWHM}_{\text{seeing}}$ is the FWHM of the atmospheric seeing (explicitly given as an input to the simulator), and $\text{FWHM}_{\text{jitter}}$ is the FWHM of the Gaussian jitter function. The

diffraction-limited point spread function is an Airy pattern with intensity

$$I(\theta) = I_0 \left(\frac{2J_1(\pi\theta D/\lambda)}{\pi\theta D/\lambda} \right)^2, \quad (8)$$

where J_1 is a Bessel function of the first kind, λ is the wavelength, D is the aperture diameter, and θ is the angular distance from the center. This means that the energy reaches half of the maximum value at $\theta = 1.61633\lambda/(\pi D)$ and therefore in arcseconds [9]

$$\text{FWHM}_{\text{diff}} = 1.028 \left(\frac{\lambda}{D} \right) (3600) \left(\frac{180}{\pi} \right). \quad (9)$$

By Eqn. 4, the FWHM of the Gaussian jitter function is

$$\text{FWHM}_{\text{jitter}} = \sigma_{\text{jitter}} \sqrt{8 \ln 2}, \quad (10)$$

where σ_{jitter} is the RMS error induced by jitter in arcsecs.

We now return to the problem of determining the ideal extraction aperture size. In practice, this is determined by iterating over a range of aperture radii r_i and calculating the total counts N_{*i} captured by each corresponding aperture using the integral of a Gaussian source profile centered at the origin given by

$$N_{*i} = N_{\text{source}} \int_0^{r_i} \frac{e^{-\frac{x^2}{2\sigma^2}}}{2\pi\sigma^2} 2\pi r dr = N_{\text{source}} \left(1 - \exp\left(-\frac{r_i^2}{2\sigma^2}\right) \right) \quad (11)$$

where $N_{\text{source}} = 10^{-0.4M_{\text{ins}}} \Delta t$ is the total source counts, Δt is the integration time in seconds, $M_{\text{ins}} = M_{\text{sat}} - M_{\text{zp}}$ is the instrumental magnitude of the satellite, and M_{sat} is its exoatmospheric magnitude. The simulated zero point is calculated from system parameters by

$$M_{\text{zp}} = 2.5 \log_{10} \left(\pi(D/2)^2 E_{\text{Vega}}(\lambda) \Delta\lambda \right) \quad (12)$$

where $\Delta\lambda$ is the spectral bandwidth, c is the speed of light, h is Planck's constant, and $E_{\text{Vega}}(\lambda)$ is spectral irradiance of Vega.

Equipped with these results, the uncertainty σ_* may be evaluated as

$$\sigma_* = 1.0857 / \max_i \left(N_{*i} / \sqrt{N_{*i} + \pi r_i^2 (N_S + N_D + N_R^2)} \right) \quad (13)$$

With Eqn. 1 and the zero point uncertainty σ_{zp} , this yields the overall theoretical photometric uncertainty.

Finally, the process by which we determine the photometric accuracy using simulated data as opposed to using theory is quite simple. Once we have the calibrated magnitudes for the target using the processing codes, we compare the input magnitude to the simulator for every frame to the processed output magnitude for each frame. We then calculate a root median square error from truth for the entire dataset to determine the simulation based photometric error.

4.2 Astrometric Accuracy

To approximate the astrometric uncertainty σ_{astro} , we evaluate the Cramér-Rao bound on the variance of an unbiased position estimate, which is [7]

$$\sigma_{\text{astro}}^2 \approx \sigma_{\text{CR}}^2 = 2\pi\sigma_{\text{PSF}}^2 \cdot \frac{B}{N_{\text{source}}^2} \cdot \left[\sum_{i=1}^n \frac{\left(\exp\left(-\frac{((i-0.5)\Delta x - x_c)^2}{2\sigma_{\text{PSF}}^2}\right) - \exp\left(-\frac{((i+0.5)\Delta x - x_c)^2}{2\sigma_{\text{PSF}}^2}\right) \right)^2}{1 + \frac{1}{\sqrt{2\pi\sigma_{\text{PSF}}^2}} \frac{N_{\text{source}}}{B} \int_{x_i^-}^{x_i^+} e^{-\gamma(x)} dx} \right]^{-1}, \quad (14)$$

where x_i is the location of pixel i , B is the total background in the pixel array, $\sigma_{\text{PSF}} = \text{FWHM}_{\text{PSF}}/\sqrt{8 \ln 2}$ is the standard deviation of the PSF, and x_c is the source location. This is the bound on a one-dimensional location

estimate, but the satellite point-spread functions explored here are azimuthally symmetric, so it should give a reasonable indication of metric error.

Like the process for the simulation-based photometric error, in order to calculate the simulation-based astrometric error we calculate the distance between the input coordinate in right ascension and declination and the processed output coordinate in right ascension and declination using the haversine formula. We then calculate a root median square error from truth for the entire dataset to determine the simulation based astrometric error.

4.3 Limiting Magnitude

Limiting magnitude may be defined and measured in various ways. One popular formulation [10] is that the limiting magnitude yields a signal of SNR 5 on the sensor. We then define predicted limiting magnitude as M_{lim} using

$$M_{lim} = M_{5\sigma} + M_{zp}, \quad (15)$$

where

$$M_{5\sigma} = -2.5 \log N_{*5\sigma} \quad (16)$$

and $N_{*5\sigma}$ is the value of total source photoelectrons giving an SNR of 5. By solving Eqn. 3 for counts, $N_{*5\sigma}$ is given by

$$N_{*5\sigma} = \frac{\text{SNR}^2}{2} + \sqrt{\frac{\text{SNR}^4}{4} + \text{SNR}^2(n_{\text{pix}}(N_S + N_D + N_R^2))}. \quad (17)$$

We can now solve for the predicted limiting magnitude, M_{lim} using Eqns. 15, 16, and 17.

In “limiting magnitude” mode, the simulator creates a second HDF5 file for every simulation case with a special limiting magnitude “ruler” consisting of a grid of pseudo satellites on $[M_{lim} - 5, M_{lim} + 5]$. The pseudo satellites are generated using the same streaking procedure and parameters as with the original input satellite(s) so that the user can effectively measure limiting magnitude for detection of that specific satellite with the given input orbit parameters. An example limiting magnitude ruler image is shown in Fig. 6 with an overlay indicating the detected pseudo-satellite grid and magnitudes.

In order to determine the limiting magnitude for detection using the pseudo satellite grid, we process the limiting magnitude ruler HDF5 file and find the magnitude threshold at which all the satellites are detected in 50% of the frames.

5. TRADE STUDIES

Having the metrics defined, we now evaluate the simulator results over various test cases along with the basic theoretical predictions.

5.1 Evaluating Limiting Magnitude Versus Read Noise

As a simple demonstration, we begin by evaluating the case of limiting magnitude versus read noise. For this analysis, we use a sample case of a geosynchronous satellite, specifically object number 39070 (TDRS 11). The observation site used was the MSSS on the summit of Haleakala. These parameters, among others, are detailed in Table 1 that gives nominal inputs used for the simulations described throughout Secs. 5.1, 5.2, and 5.3. In this case, we varied the read noise from 0 to 20 electrons and the sensor well capacity was set to 15,000 electrons.

The results for the limiting magnitude determined from the simulated data are shown in Fig. 8. Unsurprisingly, the limiting magnitude becomes significantly brighter as readout noise increases. From these data, a systems engineer could evaluate the effect of an increase in read noise from a cheaper camera system on limiting magnitude. For example, an increase in read noise from 5 electrons to 10 electrons results in a drop in sensitivity by 0.9 magnitudes which could have a large impact on a given mission.

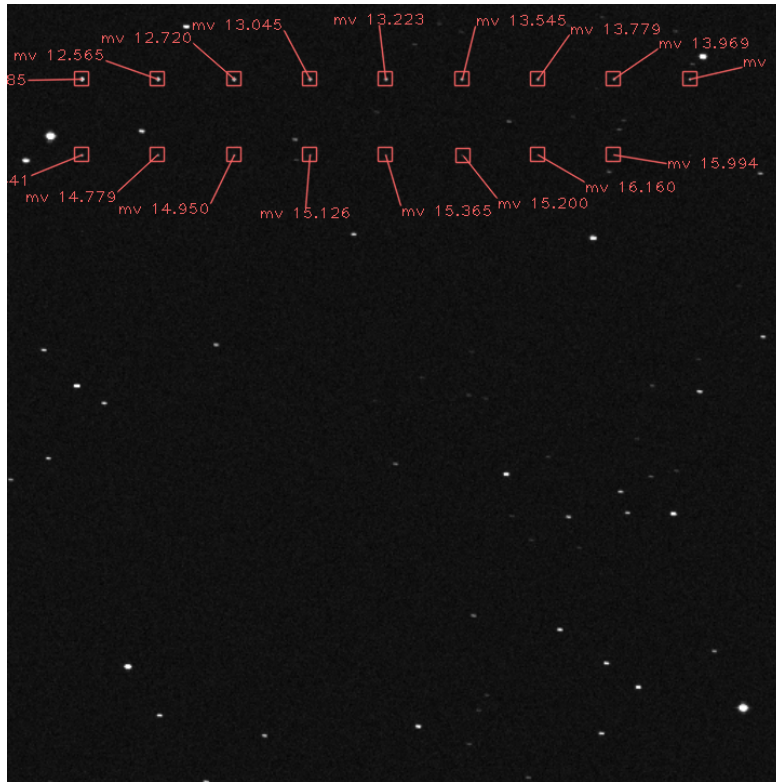


Figure 6: Limiting magnitude ruler example with pseudo satellites and visual magnitudes noted in red.



(a) no read noise added.



(b) 10 electrons.



(c) 20 electrons.

Figure 7: Example simulations from read noise cases.

5.2 Evaluating Performance Versus Aperture Diameter and IFOV Using Theory and Simulated Data

We now evaluate aperture diameter and instantaneous field of view (IFOV) to see the impact on performance metrics as predicted by theory and as observed in the simulator. The same basic system parameters summarized in Table 1 are used again, with excursions in primary mirror aperture diameter from 0.7m to 5.0 meters and IFOV from 2.0 arcseconds per pixel to 5.0 arcseconds per pixel. In these cases, the detector well capacity was set to 50,000 electrons to avoid large saturation effects. Each simulation consists of twenty seconds of data. We display the results in heat maps where each pixel of data represents one simulation run.

Fig. 9 shows the comparison between the theoretically predicted photometric uncertainty and the photometric

Table 1: Nominal Simulator Inputs

Main	Star Catalog	SSTRC6
Sensor	Latitude (degrees)	20.708
	Longitude (degrees East)	203.743
	Altitude (meters)	3075
	Output Image Size (pixels)	512x512
	Sensor Filter	Sloan i'
	FWHM of Atmospheric Seeing PSF (arcsecs)	2.0
	Camera Gain (electrons/ADU)	1
	Observation Site Background Magnitude (mag/arcsec ²)	20
	Read Noise (rms electrons/pixel/read)	10
Satellite	Object ID	39070
	Magnitude Profile Type	Periodic
	Maximum Brightness (mag)	15.0
	Minimum Brightness (mag)	15.5
	Magnitude Profile Period (seconds)	8.0 seconds
	Integration Time (seconds)	0.5
	Collection Start Date (UTC)	2017-08-04
	Collection Start Time (UTC)	12:31:35
	Collection Duration (seconds)	20

error as calculated from the simulated data. Fig 9a shows that, according to the assumptions and calculations used in Sec. 4.1, the predicted photometric uncertainty or error is dominated by primary mirror aperture diameter which makes sense due to the increase in signal provided by the increase in mirror diameter. When we look at Fig. 9b, we see some differences of note. First, the predicted uncertainty from theory is generally ≈ 0.2 magnitudes smaller than the error calculated from the simulated data because the theoretical equations do not capture star streaking and interference caused from light near the satellite in the frame. Second, the processed data in Fig. 9b shows that an increase in IFOV causes a decrease in photometric accuracy, contrary to the effects shown in Fig. 9a. This is because when the IFOV is larger, it is more likely for the target to overlap with stars in the field, corrupting the magnitude measurement.

Fig. 10 shows the comparison between the theoretically predicted astrometric uncertainty and the astrometric error as calculated from the simulated data. Fig. 10a shows that, like photometric uncertainty, astrometric uncertainty decreases with and is dominated by primary mirror aperture diameter. This result is intuitive because the increased signal from the larger mirror allows for detection of more dim stars which can then be used in the astrometric solver to improve the field solution. As for the processed simulated data shown in Fig. 10b, we notice that for the majority of the parameter space the astrometric error as predicted by the theory is quite similar to that resulting from processed data (≈ 0.1 arcsecs difference). On the other hand, theory and simulation diverge for cases with small D and large IFOV, where point-spread functions begin to overlap and the object signal becomes polluted with star photons. In addition, the Cramér-Rao bound is not tight at low SNR, therefore the divergence between theory and simulation in this region with low SNR is intuitive. We also notice that there is a slight decrease in astrometric accuracy with increase in IFOV which can be explained by the fact that the ability to centroid the source within a pixel becomes even more difficult as the PSF size gets smaller and smaller.

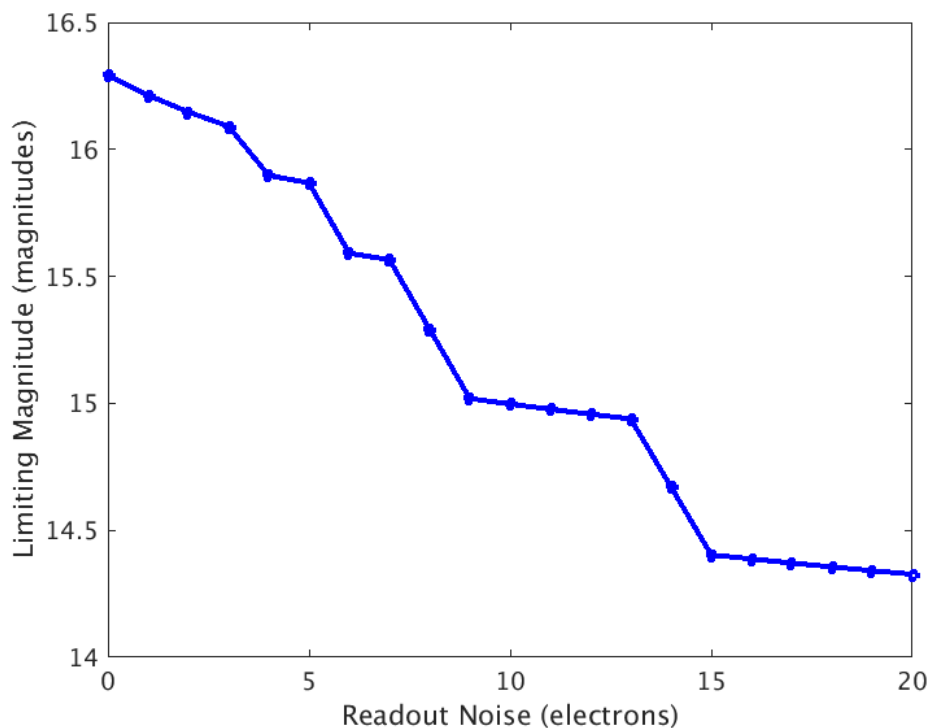
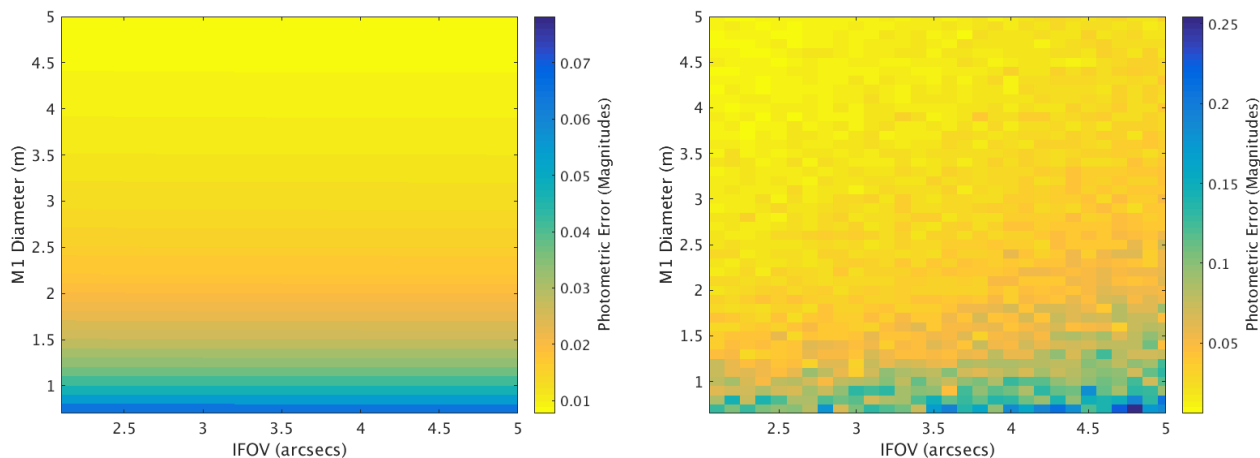


Figure 8: Limiting magnitude versus readout noise.



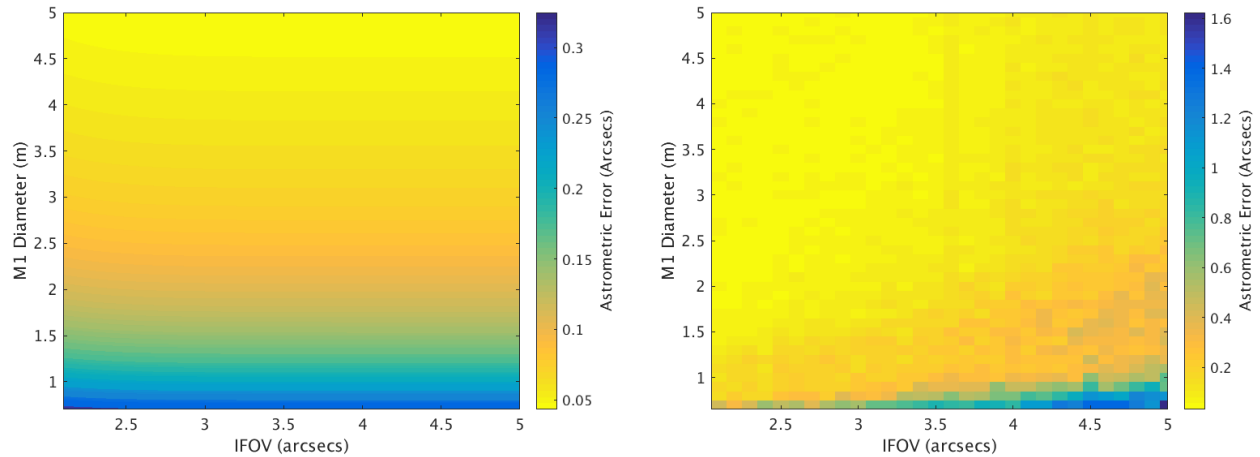
(a) theoretical satellite photometric error.

(b) satellite photometric error from simulated data.

Figure 9: Maps of satellite photometric error vs. M1 diameter and IFOV for discrete sampling points within the design space.

This effect of decreased astrometric accuracy with increased IFOV does not have as great of an impact for large aperture sizes where the signal is high.

Fig. 11 shows the comparison between the theoretically predicted limiting magnitude and the limiting magnitude as calculated from the simulated data. Fig. 11a also shows that limiting magnitude predictions from the theory as outlined in Sec. 4.3 are dominated by aperture size. As with the previous two metrics, the theoretical predictions are more optimistic than the simulated data results shown in Fig. 11b as the majority of the cases



(a) theoretical satellite astrometric error.

(b) satellite astrometric error from simulated data.

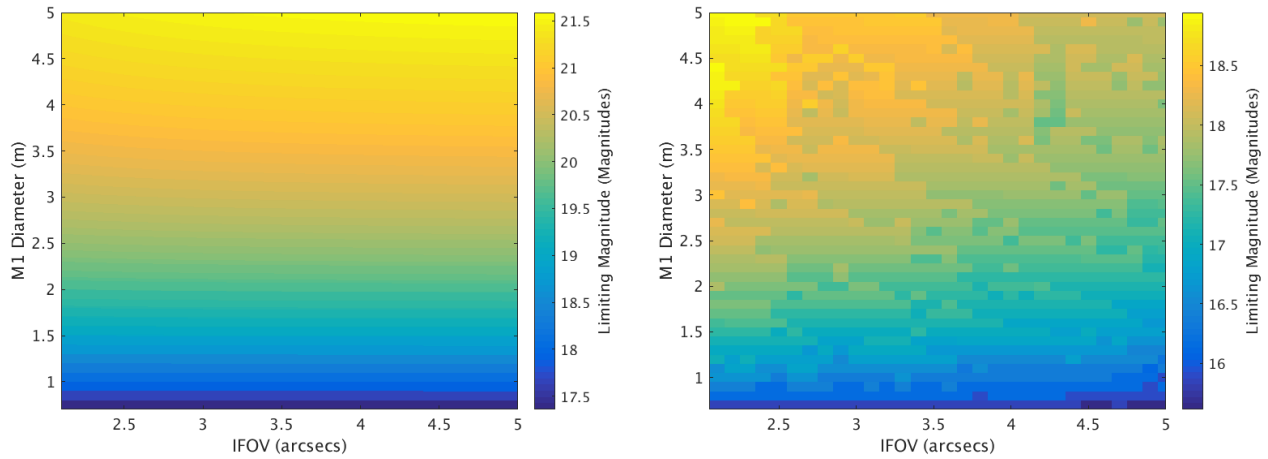
Figure 10: Maps of satellite astrometric error vs. M1 diameter and IFOV for discrete sampling points within the design space.

showed a limiting magnitude of ≈ 2.5 magnitudes brighter for the simulated case. In the simulated data case, we note that both increase in aperture and decrease in IFOV improve the limiting magnitude for the system. Increasing aperture diameter increases limiting magnitude because a larger aperture collects more light. Decreasing IFOV reduces the amount of sky noise in each pixel due to the pixel containing fewer square arcseconds and makes it less likely that object signal will be corrupted by a star. We note that these results apply to the current simulation scenario in which we have a relatively dark sky with bright objects. This result could vary over sky background and object brightness parameters, which is a potential future trade space exploration to be undertaken with simulation data. Finally, the processed data shown in Fig. 11b are less smooth than the photometric and astrometric results due to the noisy process by which limiting magnitude is inferred by the simulator.

We observe that the simulated data provides a more realistic prediction of performance metrics and reveals trends not apparent from the theory alone. This same analysis could be applied over many more observation schemes and system parameters beyond this example in order to determine trends and predict behaviors for various missions.

5.3 Evaluating Performance vs. Integration Time and IFOV at Constant Primary Aperture Diameter

In Fig. 12 and 13, we explore limiting magnitude and metric accuracy *simultaneously* as system parameters (IFOV and integration time) are varied and aperture diameter is held fixed. The system described in Sec. 5.2 is again the point of departure. In this case we use an aperture diameter of 0.5 meters, a sky background magnitude value of 18.0 magnitudes per square arcseconds, and an image size of 1024 pixels by 1024 pixels. The results reveal a subset of sensor design space in which limiting magnitude and metric accuracy are traded off in an optimal way denoted by the bound in the lower left corner of the plots but no one point optimizes both objectives [11]. Fig. 12 shows the optimal curve at the bottom left hand quite clearly. We see that the astrometric error is optimized at small IFOV and short exposure time while the limiting magnitude is optimized at small IFOV and long exposure time. Fig. 13 shows less of a defined trend as the noise in the measurement of one object (versus several used in the line-of-sight calculation) has a greater effect on the astrometric accuracy for a faint object while the limiting magnitude remains the same. These results suggest that the co-adding of short exposure frames would help provide the optimal solution for missions in which the telescope is tracking a satellite. The short exposures could be used for solving the field at optimal astrometric accuracy then the frames could be

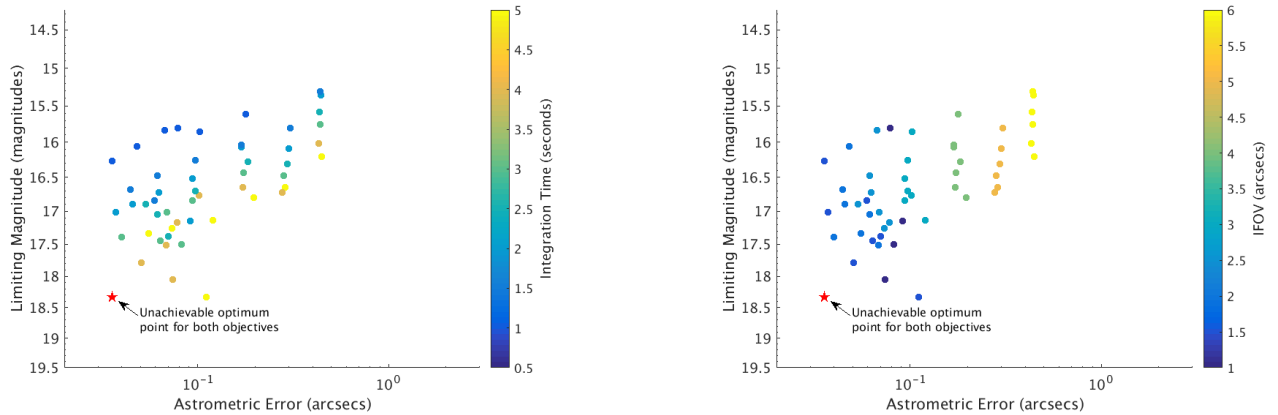


(a) theoretical limiting magnitude.

(b) limiting magnitude from simulated data.

Figure 11: Maps of limiting magnitude vs. M1 diameter and IFOV for discrete sampling points within the design space.

co-added together to detect and calculate the position of the satellite. Thus, this concept would improve limiting magnitude and detect fainter targets at higher accuracy.



(a) limiting magnitude versus line-of-sight astrometric error with integration time noted in color.

(b) limiting magnitude vs. line-of-sight astrometric error with IFOV noted in color.

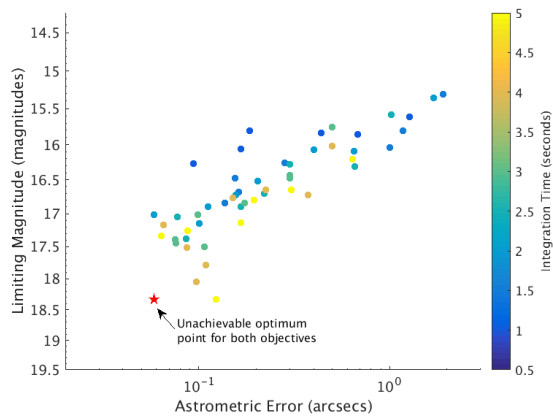
Figure 12: Limiting magnitude vs. line-of-sight astrometric error

6. CONCLUSIONS

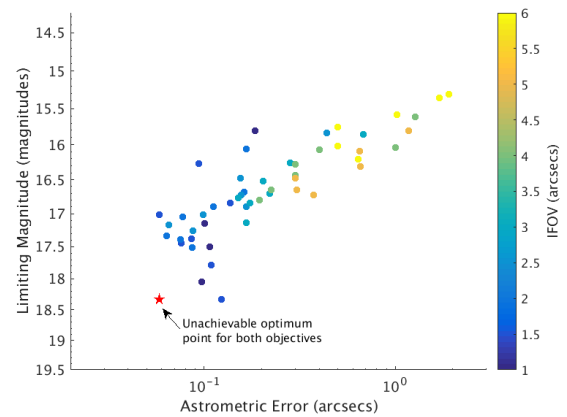
In this paper, we have presented a new tool to simulate sensor data for space object observations at the pixel level. Applied to trade space studies, it provides greater insight into predicted system performance than do simple theoretical calculations. It is also invaluable in testing data processing pipelines.

ACKNOWLEDGMENTS

This work was funded by the Air Force Research Laboratory Directed Energy Directorate through contract FA94151-16-D-0001. The authors would like to thank Michael Werth for his coding guidance in the initial



(a) limiting magnitude versus satellite astrometric error with integration time noted in color.



(b) limiting magnitude vs. satellite astrometric error with IFOV noted in color.

Figure 13: Limiting magnitude vs. satellite astrometric error

development of the simulator and Michael Abercrombie for his support in reviewing concepts and brainstorming throughout development.

REFERENCES

- [1] Bertin, E., “SkyMaker: astronomical image simulations made easy,” *Memorie della Società Astronomica Italiana* **80**, 422 (2009).
- [2] Bertin, E. and Arnouts, S., “SExtractor: Software for source extraction,” *AAPS* **117**, 393–404 (June 1996).
- [3] Lang, D., Hogg, D. W., Mierle, K., Blanton, M., and Roweis, S., “Astrometry.net: Blind astrometric calibration of arbitrary astronomical images,” *The Astronomical Journal* **139**(5), 1782 (2010).
- [4] Everett, M. E. and Howell, S. B., “A technique for ultrahigh-precision CCD photometry,” *Publications of the Astronomical Society of the Pacific* **113**(789), 1428–1435 (2001).
- [5] Howell, S. B., *Handbook of CCD Astronomy*, Cambridge University Press (Mar. 2006).
- [6] Howell, S. B., “Introduction to time-series photometry using charge-coupled devices,” *The Journal of the American Association of Variable Star Observers* **20**(2), 134–149 (1992).
- [7] Mendez, R. A., Silva, J. F., and Lobos, R., “Analysis and interpretation of the Cramér-Rao lower-bound in astrometry: One-dimensional case,” *Publications of the Astronomical Society of the Pacific* **125**(927), 580 (2013).
- [8] Hansen, E., *Fourier Transforms: Principles and Applications*, Wiley (2014).
- [9] Greivenkamp, J., *Field Guide to Geometrical Optics*, SPIE Press (2004).
- [10] Ivezić, Z., Jones, L., and Lupton, R., “The LSST photon rates and SNR calculations, v1.2,” Tech. Rep. LSE40, The Large Synoptic Survey Telescope (2010).
- [11] Coder, R. D. and Holzinger, M. J., “Multi-objective design of optical systems for space situational awareness,” *Acta Astronautica* **128**, 669–684 (2016).

APPENDIX A. NOMENCLATURE

B	total background flux ($e^- \cdot \text{arcsec}^2$)
D	diameter of primary aperture (m)
E_{Vega}	spectral irradiance ($\text{W}/\text{m}^2/\text{nm}$)
I	intensity given by Airy distribution
I_0	maximum intensity given by the Airy distribution
N	total noise for an observation (e^-)
N_*	source counts collected (e^-)
N_{*i}	source counts collected in extraction aperture of radius r_i (e^-)
$N_{*5\sigma}$	source counts collected for a 5σ collection (e^-)
N_D	dark level (electrons/pixel/integration)
N_R	read noise (rms electrons/pixel/read)
N_S	sky background level (electrons/pixel/integration)
N_{source}	total source counts (e^-)
N_{noise}	total noise (e^-)
N_{noise_i}	total noise in extraction aperture of radius r_i (e^-)
M_{ins}	instrumental magnitude (magnitudes)
M_{zp}	zero point (magnitudes)
M_{lim}	limiting magnitude (magnitudes)
$M_{5\sigma}$	5σ SNR magnitude (magnitudes)
S	total signal for an observation (e^-)
c	speed of light (m/s)
h	Planck's constant ($\text{m}^2 \text{kg}/\text{s}$)
n_{pix}	total number of pixels in extraction aperture (pixels)
n_{pix_i}	total number of pixels in extraction aperture of radius r_i (pixels)
r_i	radius of a given extraction aperture instance i (pixels)
r	dimensionless distance from center of focal plan in Airy distribution
x_i	location on pixel detector at pixel index i (arcseconds)
x_c	source location on pixel detector (arcseconds)
x	location on pixel detector (arcseconds)
FWHM	full width half max of Gaussian
FWHM _{diff}	full width half max of the diffraction limited point spread function (arcseconds)
FWHM _{seeing}	full width half max of atmospheric seeing (arcseconds)
FWHM _{jitter}	full width half max of Gaussian jitter function (arcseconds)
FWHM _{PSF}	full width half max of point spread function (arcseconds)
SNR	signal to noise ratio
SNR _{i}	signal to noise ratio of observation with extraction aperture size of radius r_i
σ	standard deviation of a Gaussian distribution
σ_*	uncertainty of a given measurement (magnitudes)
σ_{jitter}	standard deviation of the Gaussian jitter function (arcseconds)
σ_{PSF}	standard deviation of the point spread function (arcseconds)
σ_{photo}	photometric uncertainty for a given observation (magnitudes)
σ_{photoADU}	photometric uncertainty for a given observation (e^-)
σ_{astro}	astrometric uncertainty (arcseconds)
σ_{zp}	uncertainty of a given zero point measurement (magnitudes)
σ_{CR}	Cramér-Rao bound on positional estimate (arcseconds rms)

$\gamma(x)$	flux at a given pixel with location on the detector x (e^-)
λ	light wavelength (meters)
θ	angular radius of Airy function (radians)
θ_{FOV}	field of view of sensor (degrees)
$\Delta\lambda$	bandwidth of light analyzed (meters)
Δt	integration time (seconds)

DISTRIBUTION A. Approved for public release: distribution unlimited.